International Journal of Impact Engineering 180 (2023) 104663

Contents lists available at ScienceDirect

International Journal of Impact Engineering

journal homepage: www.elsevier.com/locate/ijimpeng

Low-velocity impact behavior of elliptic curved composite structures

J. Gebhardt [a], M. Schlamp [a], I. Ehrlich [a,*], S. Hiermaier [b]

[a] Labor Faserverbundtechnik, Ostbayerische Technische Hochschule Regensburg, Prüfeningerstraße 58, 93049 Regensburg, Germany
[b] Fraunhofer-Institut für Kurzzeitdynamik, Ernst-Mach-Institut, Ernst-Zermelo-Straße 4, 79104 Freiburg, Germany

ARTICLE INFO

Keywords:
Impact damage
Impact behavior
Curved composite
Numerical model
GFRP

ABSTRACT

Although many composite structures are inconsistently curved, such as the leading edges of aircraft wings, the variety of research in impact engineering is almost limited to the impact performance of plates or cylindrically curved specimens. It is not known whether the findings obtained from standardized tests can be transferred to curved structures or which adaptions are required. Therefore, a deeper understanding of the deformation and damage behavior of inconsistently curved structures is essential to transfer the observed impact behavior of flat specimens to general curved structures and therefore to utilize the full lightweight potential of a load-specific design. An accurate description of the procedure as well as the results of the experimental and numerical study of the low-velocity impact behavior of differently single-curved elliptic specimens is presented. To close the research gap of the impact behavior of geometries with curvatures between the plates and simplified leading edges, novel specimens geometries have been derived from established impact test standards. Glassfiber-reinforced specimens are subjected to an instrumented impact test at constant impact energy. This is numerically investigated by a stacked-layer model, which used cohesive zone modeling to enable the simulation of matrix cracking, fiber fracture and delamination. The resulting projected damage areas, as well as the force and deflection histories, were evaluated and section cuts were examined to discuss the damage morphology, formation and propagation process. Significant effects on maximum deflection, compliance and dynamic behavior on the size and morphology of damage were found.

1. Introduction

In structures made of composites, such as aircraft wings, a potential collision with solids or other low-energy impact scenarios must be expected during regular operation. Such impact damages occur on a moving aircraft during takeoff and landing, primarily on parts that face in the movement direction, such as wing leading edges, the leading edges of the engines or pitch elevators and side rudders. Due to aerodynamic reasons, these structures have an approximated elliptical cross-section and are supported with stiffening elements to achieve a load-compatible design. The increasing use of fiber-reinforced composites for weight reduction has increased the importance of predicting the severity of impacts. The damage mechanisms of composites are complex due to the inhomogeneous stacking of several anisotropic layers, and resulting damages inside the structure are often not or hardly visible from the outside. Under certain circumstances, these impact scenarios can cause a Barely Visible Impact Damage (BVID). It must be ensured that their effects do not cause any progressing damage until they are detected in regular maintenance.

BVIDs can reduce the laminates load-carrying capabilities drastically by delamination formation, matrix cracking, and in severe cases, fiber failure inside the structure [1,2]. Designers of composite structures require an improved understanding of how laminates respond to impact loads which do not cause visible damage to make use of the materials full lightweight design potential. Different modes of damage may occur during an impact event at varying locations within the structure, whereby the damage modes are interacting. The final morphology of the damage is dependent on several structure-inherent parameters like the geometric shape of the structure, the predominant boundary conditions, the laminate lay-up, the resulting thickness and the material of the single-layers. Out of plane impact scenarios are characterized by the impactor material, the impactor mass and the impactor velocity [3,4]. An example for a typical damage propagation mechanism is the initiation and interaction of delaminations with matrix cracks.

* Corresponding author.
E-mail addresses: jakob.gebhardt@oth-regensburg.de (J. Gebhardt), ingo.ehrlich@oth-regensburg.de (I. Ehrlich), Stefan.Hiermaier@emi.fraunhofer.de (S. Hiermaier).

https://doi.org/10.1016/j.ijimpeng.2023.104663
Received 13 February 2023; Received in revised form 19 May 2023; Accepted 21 May 2023
Available online 7 June 2023

In the contact area of the impactor, cone-shaped damage is initiated by intralaminar matrix cracks or by bending stresses on the opposite laminate side that subsequently propagate [1,4–6].

1.1. Significance and scope

The impact behavior of fiber-reinforced composite panels and their residual load bearing capacity has already been researched intensively. The low-velocity impact behavior of curved composite structures was investigated primarily on different cylindrical curved specimen [7–12] and airplane panels [2,13–15]. Literature concerning the low-velocity impact behavior of inconsistently curved composite structures, like in this work, only addresses numeric evaluation of bird-strike events by means of smoothed particle hydrodynamic bird models [16,17]. It is generally accepted that delamination threshold loads (DTL), evaluated from sudden load drops found in force-time histories of out-of-plane impact loads of plate-shaped specimens are indicators for the laminate's capability to resist impact damage. This might be useful in a damage-tolerant design concept of actual composite structures [18]. Up to this day there is still no uniform and established method for transferring the damage tolerance of flat plates to curved structures.

This work considers the research gap of the impact behavior of differently elliptically curved composite structures on the basis of tests, whereby the geometry is varied from flat half-ellipses to strongly elliptically curved specimens. The investigation is addressed in an experimental-numerical approach to evaluate the influence of the geometry on the transient impact behavior and damage formation.

1.2. Impact of curved composites

Ambur and Starnes [7] studied the response and failure characteristics of cylindrical curved, quasi-isotropic laminates made from graphite-epoxy. They subjected curved 16-ply-thick and 8-ply-thick $[+45/0/-45/90]_{ns}$ laminates to low-velocity impact of about 2 J by a 1.13 kg drop-weight impactor with a hemispherical tip of 12.7 cm diameter. The specimens had the outer dimensions of 22.86 cm by 12.7 cm and a height determined by the radii 38.1 cm, 76.2 cm and 152.4 cm. It is concluded that for cylindrical curved specimens subjected to a constant level of impact energy, the contact force depends on the laminate thickness and the curvature radius. As the radius of curvature increases, the maximum contact force decreases (lowest and medium-high geometry) and then increases (medium-high sample to highest geometry).

Kim et al. [9] performed a three-dimensional numerical analysis of CFRP plates and curved shells to study the dynamic behavior, the effects of different lay-ups and the impact-induced damage. The geometrical model with the length and width of 8 cm and radii 5 cm, 10 cm, 100 cm and ∞ cm (a plate) with the lay-ups $[0_4/90_4]_s$, $[90_4]_s$ and $[+45_4/-45_4]_s$ is simply supported on all edges. One eight-noded brick element through thickness is used to represent a group of four neighboring plies with the same fiber orientation. To model failure, matrix cracking is predicted by Hashin's [19] failure criterion and a semi-empirical ellipsoidal delamination-criterion assuming delamination initiation by matrix cracking. It has been observed that increased contact forces are caused by a higher curvature of a cylindrical composite shell and that the delaminated areas of the cylindrical shells are larger than those of plates at the same impact speed.

Krishnamurty et al. [8] predicted the impact response and damage in large laminated composite cylindrical shells by finite element methods.

The FE-Code takes matrix cracking, fiber breaking and delamination as well as a reduction of the stiffness of the failed lamina into account as suggested by Choi and Chang [5,20,21]. The effects of impactor mass and velocity and geometric non-linearity is included. Effects of simply supported or clamped boundary conditions were found to be important to the impact response of curved laminates. Simply supported edges induced higher impactor deflections and consistently more flexible responses whereas clamped boundaries induced stiffness. An increased curvature (the reciprocal of the tangential radius of the arc section) resulted in lower deflections and contact times, while the maximum contact forces increased only slightly. It is suspected that dynamic deformation waves generated by the impact, which are reflected by boundaries, alter the course of contact force after maximum contact force.

Kumar et al. [10] studied the effect of impactor parameters and laminate lay-up on the impact response and impact damages in cylindrical curved laminates with the 3D finite element software ANSYS/LS-DYNA. Orthotropic and quasi-isotropic laminates were considered. Again the proposed damage-criteria for matrix cracking and delamination according to Choi & Chang [22,23] were used to account for direction dependent stiffness reduction of the failed elements. It was shown that a degradation of the stiffness corresponds with an increasing shell deflection, a reduction of the maximum contact force and the increased extent of matrix cracks and delamination whereas the greatest extent of the delamination area corresponds with the fiber direction of the impact-averted side. The increased curvature induced an increased maximum impact force and a reduction of the amplitude caused by natural oscillations for which a curvature stiffening effect is found to be accountable. A damage mechanism induced by the matrix cracks in the bottom-most ply, due to bending stress, and subsequent Mode I inter-laminar tensile fracture was identified from damage criterion evaluation.

Short et al. [12] presented an experimental study of the compression after impact strength of flat and curved glass fiber reinforced plastic (GFRP) $[0/\pm45/0]_s$ laminated panels. The specimen were subjected to instrumented 6 J low velocity impact tests clamped within a square 40 mm window. A set of laminates was solely used for impact damage inspection by thermal de-ply, cross-sectioning and micrography, neglecting CAI testing. The projected impact damage area determined by light transmittance method for a curved laminate was found to be greater than that for flat ones whereas the individual delamination shapes found by thermal de-ply are comparable. The cross-sections show a pine-tree damage pattern whereas no drastic effects of different curvatures were found.

Ehrlich [24] investigated quasi-isotropic plates and shallow curved CFRP specimens regarding their impact and damage behavior with both concave and convex curvatures. It turned out that convexly curved test specimens induce significantly greater damage than flat and concave specimens showing less damage than flat specimens. Even a slight curvature is sufficient to achieve a shell-like stress state. Introduced transversal loads are not only beared by lateral forces and moments but also by membrane forces. The membrane stresses caused by the shell influence the proportion of transversal shear stresses and therefore the delamination area.

2. Experimental setup and numerical model

By simplifying the generalized wing cross-section to a symmetrical semi-ellipse, the influence of the curvature on the impact behavior can be determined by laboratory-scale experimental studies. Ellipses are generally defined as a special case of a conical cut section with axis-parallel symmetry axes. With the center point $(y, z) = (0, 0)$ of the ellipse in the origin of the considered coordinate system, the center-point equation of an ellipse is

$$b^2 y^2 + a^2 z^2 = a^2 b^2, \tag{1}$$

where the symmetry axes y and z coincide with the semi-axes a and b. The width of the elliptic section between the clamps is chosen to be $2b = 100$ mm based on the plate dimensions of the standards DIN 6038 [25] and ASTM D7137 [26]. The dimension of the second half-axis is varied between $a = 25$ mm and $a = 100$ mm in steps of 25 mm.

The specimens are designated on the basis of the dimensions of the length a of the varied semi-axis of the elliptical shape, whereas the

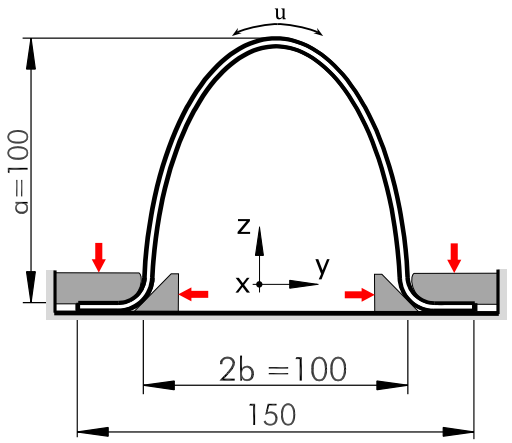

Fig. 1. Exemplary representation of specimen geometry E100, the circumferential direction u and the schematic clamping device.

Table 1
Specimen labeling and geometry parameters.

Label	a	b	u	κ
–	in mm	in mm	in mm	in mm^{-1}
E25	25	50	121	0.01
E50	50	50	157	0.02
E75	75	50	198	0.03
E100	100	50	242	0.04

length b of the second semi-axis is constant. The maximum lateral width and length of the specimens is 150 mm, derived from above-mentioned standards. The lateral flat sections of two EN6038:2015.2016 specimen edges in Fig. 1 are added to clamp the specimen. The curvature κ refers to the inverse circle of curvature R of the main apex

$$\kappa = \frac{1}{R} = \frac{b}{a^2} \tag{2}$$

and the circumferential length u is considered regarding the convex surface, starting at the apex, as indicated in Fig. 1.

Table 1 summarizes the investigated geometric parameter combinations.

2.1. Experimental procedure

All specimen used in this work were made of Sigrapreg G U300-0/NF-E320/35% unidirectional GFRP prepreg by the company SGL Carbon [27] with the fiber direction 0° along the circumference and 90° in parallel with global x-direction. The quasi-isotropic $[+45/0/-45/90]_{4s}$ laminate, with [+45] on the outsides, is stacked in convex aluminum molds which are vacuum bagged and cured by the supplier's recommended autoclave process. After curing, the edges of the specimens were trimmed with a diamond saw to fit the lateral dimensions as stated above.

For impact testing, each specimen was fixed with a specifically designed device on the base of the drop tower so that a lateral clamping without pretension in the plane was assured, as shown schematically in Fig. 1. After the impact test the outline of a damage area was marked on a translucent foil using a strong 14.4 W LED of the company Bresser underneath the semi-transparent specimen. The actual area is then quantified by the help of the light microscope Keyence VHX-5000 and the software VHX Ver. 1.3.2.4. This procedure allows the adequate determination of the projected damage areas despite the varying curvature along the circumference. After impact small specimen were cut out by a diamond saw for the determination of the fiber volume content according DIN EN ISO 1172 [28].

The position of the delaminations through-thickness as well as the propagation in the circumferential direction is of particular interest to investigate the effects of the geometry. The section cuts are created in the plane of curvature through the centrally located impact point.

2.2. Instrumented impact testing

The impact is generated by a rail guided, otherwise free-falling, mass with a frontally mounted hemispherical indentor of $D = 16$ mm diameter to provide defined and consistent impact conditions according to DIN EN 6038-1 [25] and ASTM D7136 [26]. The total mass of the drop-weight is 864 g. The adjustment of the measured kinetic impact energy, i.e drop-weight and target impact velocity, is controlled by the distance between drop height and specimen vertex. Due to the high accelerations and the dynamic process a piezoelectric force transducer is instrumented.

A load cell PCB 208C05 is bolted in between the carriage of the drop-weight and the indentor. The frequency resolution is theoretically limited by interferences of natural resonances and the AD-Converter. The load cell contains current-to-voltage transformation electronics, which are supplied by a signal conditioner. A NI 9223 AD-Converter with 16 Bit and 1 MHz resolution is used to convert the analog force-proportional signal.

The course of the impactor velocity, the displacement and the energy transmitted to the specimen is calculated according to ASTM D7136 [26]. The absorbed energy $E_a(t)$ is calculated by the measured transient contact force $F(t)$ using numerical methods to integrate the signal. With the initial impact velocity v_i, the drop mass m and the gravitational acceleration g, the velocity $v(t)$ of the impactor is

$$v(t) = v_i + gt - \frac{1}{m}\int_0^t F(t)\,dt \tag{3}$$

and the deflection-time history $\delta(t)$ is

$$\delta(t) = \delta_i + v_i t + \frac{gt^2}{2} - \frac{1}{m}\int_0^t \left(\int_0^t F(t)\,dt\right) dt. \tag{4}$$

With the course of the velocity $v(t)$ and deflection $\delta(t)$ during the impact process, the energy $E_a(t)$ transferred to the specimen is considered by the kinetic and potential energy components

$$E_a(t) = \frac{m\left(v_i^2 - v(t)^2\right)}{2} + m\,g\,\delta(t). \tag{5}$$

The part of kinetic energy transferred to damage formation is $E_a(t_i)$ whereas t_i is the time step the impactor lost contact and the force drops to zero $F(t_i) = 0$. It is assumed that the impactor is always in contact with the vertex of the specimen.

2.3. Numerical model

A first numerical model of the experimental impact test was set up in Ls-Dyna to further investigate the impact behavior of the elliptically shaped specimen. The transient contact force, the displacement and the ratio of maximum extent of damage is compared to the actual impact test results. Furthermore, the effect of damage formation to the force time curves is investigated by neglecting failure in a second numerical study.

2.3.1. Global/local mesh strategy

To reduce the number of elements and therefore for computational time reduction a solid/shell modeling technique, like shown by Sun and Hallett [2], was applied by separating the geometry in two distinguished meshing regions [2,13]. A central impact region with solid-elements is used to represent the individual plies including a cohesive-zone model of the bonded plies. The surrounding linear-elastic region consists of shell elements used to introduce the boundary conditions. These regions are coupled by a transition part of solid elements, see Fig. 2(a).

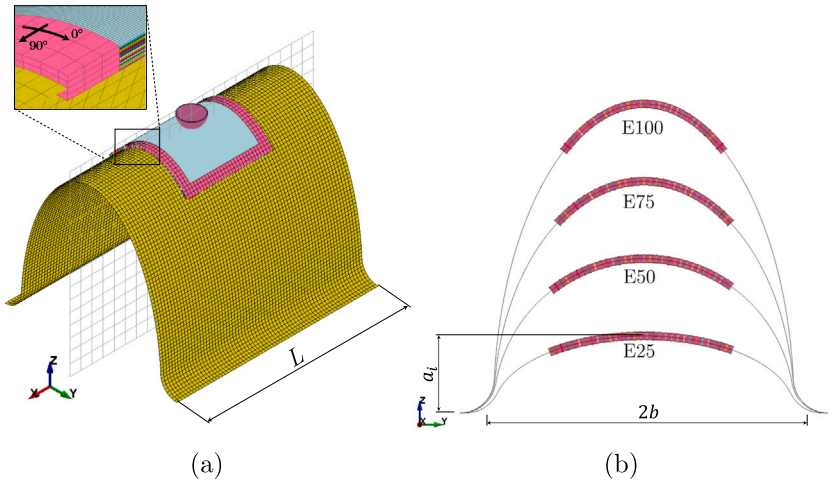

Fig. 2. (a) Isometric view of model E100 and detailed section of the implemented solid/shell modeling approach and (b) stacked side-view of all geometries used in the numerical investigations.

With the knowledge of the extent of damage from the experiment, the size of the region of interest was chosen to be 25 mm around the impact point. A central square area of 50 mm length in circumferential and 50 mm in global × direction was meshed with one element through thickness per ply to ensure a constant element size. The elements on the edges of the central region were connected to the transition part through tied-surface-contact conditions. To connect 16 plies of solid elements with a single shell, a transition part with 4 solid elements through thickness was included. The connection between the transition part and the shell was established by nodal rigid bodies to constrain nodes on a line through thickness and to enforce rotational and translational continuity, conforming with thin shell theory [2].

The nominal element size in the fine meshed solid region of interest was (0.25 × 0.25 × 0.156) mm, only with small deviations through thickness due to the curved geometry. All shell elements and the elements of the transition zone had the dimensions (2 × 2) mm. The latter were 0.625 mm thick. This meshing strategy resulted in 1.192 million nodes in the region of interest for every geometry, 2160 nodes in the transition part and in between 3845 for geometry E25, to 8218 nodes for geometry E100, in the shell region.

2.3.2. Materials and parameters

The clamping of the test set-up was represented in the numerical model by constraints of the undermost nodes of the specimen geometry, see Fig. 2(b). The impactor is a rigid (Mat_2) hemisphere, initially in contact with the topmost solid layer. To introduce the kinetic energy of 7 J, the initial velocity $v_i = -4.034$ m/s and the mass of the impactor is adjusted according to the actual impact test. To provide a proper bending stiffness in the elastic regime, element formulation 1 and Belytschko–Bindeman [29] assumed strain co-rotational stiffness form hourglass control (type 6) with a coefficient of 1.0 is used for all solids. Due to the fact that only one element over the thickness is used per ply it is likely to observe hourglassing when the elastics constants are degraded after failure occurs and further deflection is induced. Therefore, the results were critically examined for plausibility and the proportion of hourglass-energy per part was checked and found to be negligible.

The local orthotropic material axes were defined by rotating the material axis about the element normal by the angle of the ply. The normals of the elements point in the direction of the concave side of the elliptic geometry. Matrix crushing, fiber crushing, shear failure and the delamination criterion in Mat_22 are suppressed by high strength values of 1 GPa. Delamination is implemented by cohesive zone modeling. The degradation scheme for the elastic moduli of the material model is $E_1 = 0$ in case of fiber failure, which is calculated according to the Chang & Chang [22,23] failure condition, and $E_2 = G_{12} = 0$ in case of tensile matrix failure [30]. Therefore, Mat_22 accounts for fiber failure and matrix cracking which is an approximate simplification of the three-dimensional failure mechanics and sufficient to reveal dominant failure modes anticipated in the low-velocity impact case of thin laminates.

Table 2
Material parameters and interface properties.

Material properties of Mat_22	Ud-GFRP
Longitudinal modulus E_1	45.075 GPa
Transverse modulus E_2	10.540 GPa
Through-thickness modulus E_3	10.540 GPa
Poisson's ratio ν_{12}	0.276
Poisson's ratio ν_{13}	0.276
Poisson's ratio ν_{23}	0.3
Mass density ρ	2000 kg m^{-3}
Shear modulus G_{12}	3.804 GPa
Shear modulus G_{23}	3.76 GPa
Shear modulus G_{13}	3.804 GPa
Bulk modulus of failed material K_f	2 GPa
Tensile strength in fiber direction X_T	1300 MPa
Transverse tensile strength Y_T	80 MPa
Material properties of Mat_2	IMPactor
Young's modulus E	210 GPa
Poisson's ratio ν	0.3
Mass density ρ	7890 kg m^{-3}
Interface properties of tiebreak	Interlaminar
Mode I failure stress limit	80 MPa
Mode II failure stress limit	150 MPa
Mode I energy release rate	1.139 N/mm
Mode II energy release rate	2.61 N/mm
Contact Stiffness CN	50 GPa

Different types of zero-thickness discrete cohesive elements and cohesive contacts are available in Ls-Dyna to represent initiation and propagation of delamination [31,32]. The considered model is governed by a quadratic delamination-initiation criterion, a mode specific bilinear traction separation law, based on release rates, and a strength-based softening. Tiebreak contacts with the definition of contact sets are used to ensure the correct evaluation of the through-thickness stresses in terms of compression and tension.

To represent the boundary zones between individual single plies, automatic one way surface based tiebreak contacts are included to reveal possible delaminations. Tiebreak contact type 9, which is derived from Mat_138, is used with a stiffness ratio of unity and the material parameters in Table 2 without damping. A bilinear traction–separation law governs the damage formation. The material parameters were determined by numerical calibration using experimental results of

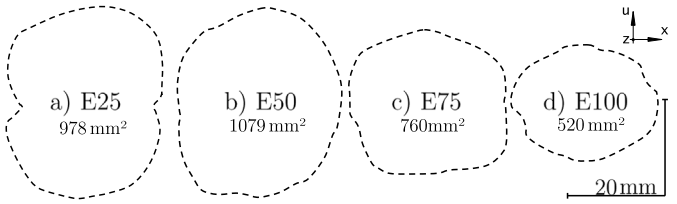

Fig. 3. Experimentally determined projected delamination boundary of the geometry (a) E25, (b) E50, (c) E75 and (d) E100.

double cantilever and end notched flexure tests as well as analytically corrected beam theory calculations. Element formulation 2 is used for all shell elements with the shear correction factor 5/6 [31], five integration points and hourglass control type 4. The three-dimensional position of the failed tied contact is evaluated in respect to the coordinate system of the undeformed geometry whereas experimentally determined delamination shapes were evaluated in a projection view regarding the specimen's surface.

3. Results and discussion

The high repeatability of the experiments allows that in this work only one representative copy per geometry is displayed. The cured specimens are nominally 2.75 mm thick and the average fiber volume fraction is 61.8%.

3.1. Impact test analysis

In the following, the maximum damage area extent in the circumference $\bar{u} = u_{max} - u_{min}$ and in parallel to the apex $\bar{x} = x_{max} - x_{min}$, according to the coordinate system shown in Fig. 4, is highlighted.

Fig. 3 depicts projected maximum damage extents of one specimen of every geometry investigated prior to cross sectioning. The centrally located and more translucent, eventually undamaged, ring was neglected in failure area determination. This observation is familiar from plates damage morphology and is caused by compression of the laminate by the impactor, which restrains crack opening [33] in an downwards opening conical segment [6].

In general, the damage area A decreases from Fig. 3(a) to (d) whereas the specimen curvature increases. A slight difference in between the delamination area of specimens E25 and E50 does not comply with this first observation. The increase of the damage area from E25 ($A = 978\,\text{mm}^2$) to E50 ($A = 1079\,\text{mm}^2$) is followed by a pronounced decreasing damage area of E75 ($A = 760\,\text{mm}^2$) and E100 ($A = 520\,\text{mm}^2$) which was also shown by Schlamp [34].

The deviations are mainly established by a decreasing trend of the maximum extent of the damage area $\bar{u}$ in circumferential direction with increasing curvature whereas the extent $\bar{x}$ increases slightly.

Fig. 4 depicts the positions of delaminations and matrix cracks of representative specimen reproduced from cross-sections examined by digital microscopy. For all examinations, it applies that the area directly under the impact site shows less delaminated interfaces than the adjacent area. The through-thickness delamination density decreases from there on, in the circumferential direction u.

The maximum circumferential damage extent is determined by three leading delaminations, Fig. 4(a) and (b), or two leading delaminations, Fig. 4(c) and (d), leading delaminations and increases with decreasing curvature. These leading cracks were always situated above a [0]-ply, except for the topmost leading crack in Fig. 4(d), which was situated underneath a [0]-ply. Apart from the mentioned outlier, this damage morphology might be explained by bending stiffness variations throughout the laminate thickness, that explains the formation of the peanut-shape [35] delamination formation of composite plates. Because the bending stiffness is primarily dependent on the fiber direction,

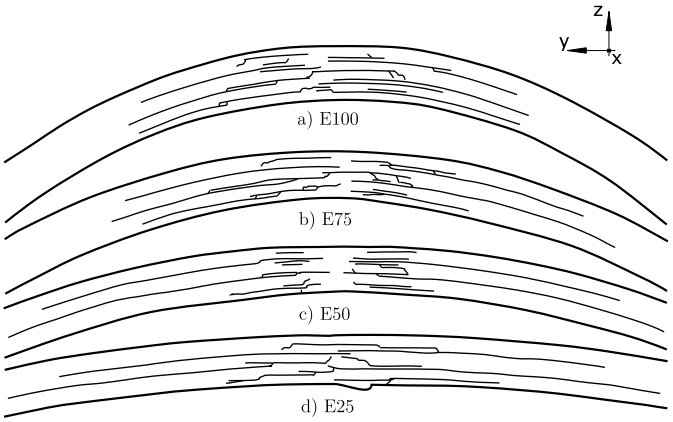

Fig. 4. Delamination and matrix cracks of specimen with geometries (a) E100, (b) E75, (c) E50 and (d) E25.

a bending stiffness mismatch of a [±45/0]-interface promotes mode 1 crack tip opening in 0°-direction by local concave bending of the bottom [0] ply and more flexible local bending of the top [±45] ply. The inverse, crack restraining, effect takes place at the [0/±45]-interfaces. The higher the curvature of the specimen, the more centralized the damage appears. At least in the cross-section plane, the topmost ply does not exhibit any matrix cracks whereas the bottom most ply is cracked at least once. This observation is also valid for general visual inspection of the specimens. The compliance of all geometries is large enough to prevent breakage due to contact-induced stresses between the impactor and the first layer of the laminate whereas the large deflection induce matrix cracking due to bending.

3.2. Impact simulation damage analysis

The modeling strategy with discrete cohesive zones and single-layer modeling was chosen to map the dominant failure modes and predominant damage mechanisms. The determined elements which degraded due to matrix cracking of all four geometries are shown in Fig. 5. The coloring corresponds to the 16 different individual layers. Depending on the orientation of the ply and the transverse stress of the elements, matrix fractures increasingly occurred at layers with a [±45] orientation whilst almost every ply exhibited matrix failure.

The total number of failed elements was inversely related to the projected delamination area. While the geometry E100 showed the most interfiber failure, the proportion of the geometry E50 was the lowest. This is an indication for a shift of energy transferred from interlaminar damage to intralaminar damage with increasing curvature. The propagation of damage in circumference was the widest in the bottommost [−45] single layer of geometry E100. According to the numerical results, damage starts with early matrix cracks on the lower, impact opponent side plies. The number of elements failing due to matrix fracture increases dramatically just before the contact force approaching the DTL, resulting in a widespread failure across all layers.

3.3. Instrumented impact test data

Fig. 6 depicts the experimental and numerical results of the impact tests. The numeric contact force Num. $F(t)$ is extracted from database *rcforc* by an implemented force transducer contact of the indenter and the displacement Num. δ is sourced from database *matsum*. The force measurement results Exp. $F(t)$ of and the experiment are filtered with SAE 8000 but the experimental deflection Exp. $\delta(t)$ is calculated from unfiltered data according to Eq. (4). The numeric results are not filtered.

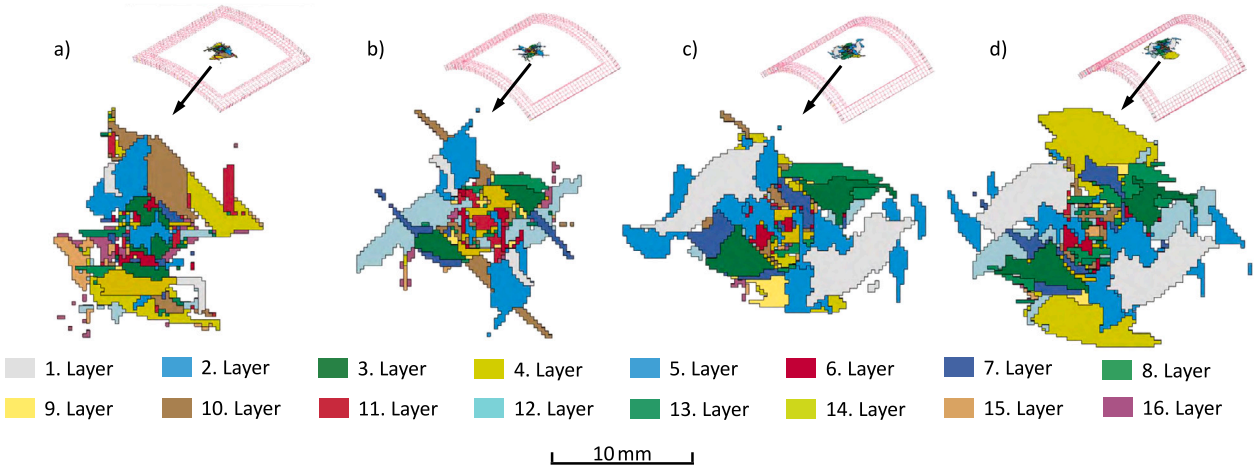

Fig. 5. Elements failed due to matrix cracking of the geometry (a) E25, (b) E50, (c) E75 and (d) E100.

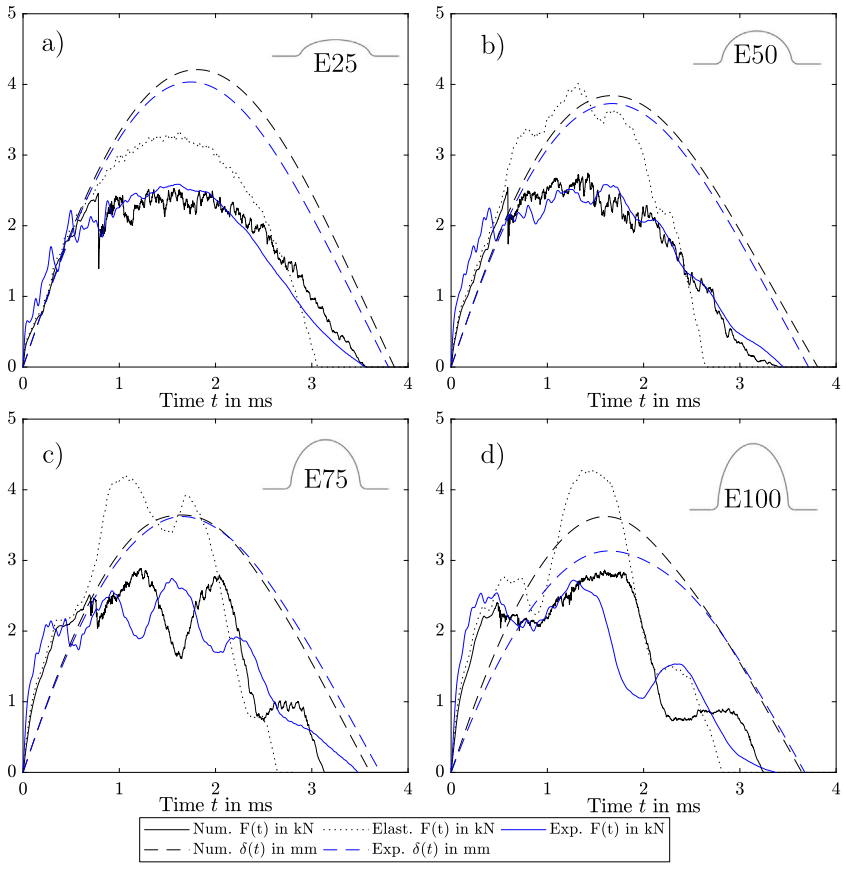

Fig. 6. Comparison of transient experimental (Exp.), numerical with damage (Num.) and numerical linear-elastic (Elast.) force $F(t)$ and displacement $\delta(t)$ results for the geometry (a) E25, (b) E50, (c) E75 and (d) E100 at 7 J impact energy.

Besides the numeric results Num. $F(t)$ incorporating damage, results from linear-hyperelastic calculations Elast. $F(t)$ without failure criteria are displayed to evaluate influence of damage formation, which is not physical, but reflects the dynamic structural behavior.

The numerical models reflected the course of the transient contact force $F(t)$ and deflection $\delta(t)$ of the experiments with sufficient accuracy. In the initial phase of increasing contact force $0 < t < 0,5$ ms, it can be seen that the numerical models respond less stiffly than the actual specimens. This more compliant behavior was especially dominant in the further force curve after $t > 0.5$ ms whereat the lateral higher specimens E75 and E100 in Fig. 6(c) and (d) induced vibrations with frequencies lower than indicated by the experiment. Therefore, the evaluation of e.g., the impact duration must be treated with some reservation, with respect to the specimens' geometry. The detachment of the impactor from the specimen vertex is distorted by natural vibrations. This becomes even more effective with an increasing length of the unwound circumference u.

The determination of a delamination threshold load by mere visual inspection of the experimental force-time histories is not certain since differences between force drops due to specimen vibration and force

drops due to damage formation are not distinct and no method for determining the DTL in this case is established. There are at least three sources of oscillations of the force signal which might occur superposed. These are the excited natural frequencies of the tested structure and the impactor and the actual load drops due to a DTL, which all are superimposed and blurred by the mass-inertia of the impactors cap in between the load cell and the specimen.

The numeric model is used to find and understand delamination formations. A result of the numerical model is the transient contact force curve. The rather flat, mildly curved, test specimens E25 and E50, see Fig. 6(a) and (b), show distinct force drops whereas the DTL is less pronounced at higher curvatures E75 and E100, see Fig. 6(c) and (d).

Another observation is that although the most curved specimen E100 shows the less pronounced DTL, multiple load drops are present which correlate with delamination expansion, as observed in the numerical models. One reason for this could be the natural frequencies, which lead to time-dependent deformation. Due to the global bending caused by the deformation in the excited normal mode, which does not necessarily lead to an increased contact force, further interlaminar stress is induced. This may result in further delamination initiation and propagation in superposition with the local bending, caused by the impactor.

In Addition, Fig. 6 shows the linear-elastic calculation results for the theoretical contact force Elast. $F(t)$ without damage. The initial linear-elastic regime in between the initial contact and before the first DTL is in accordance with the numerical results including damage. After the corresponding time steps of the first DTL, Elast. $F(t)$ rises quickly, because the excited vibration of the structure results in a movement of the vertex against the impactor movement direction. The modal effective masses of the corresponding normal mode increase with the lateral height of the geometry such that the natural frequency decreases and the resulting amplitude of the contact force increases. This supports the assumption of the role of normal mode deformation mentioned above.

The course of the deflection Exp. δ and Num. δ shown in Fig. 6 agrees reasonably well. It can be seen that with increasing curvature of the specimens the maximum deflection decreases as well as the delamination area decreases by trend. Therefore, the effect of geometric compliance, resulting in higher deflections, is in accordance with a delamination area formation, which supports the assumption of bending dominated delamination propagation. Due to the chosen specimen design, the most curved specimen E100 exhibits the highest elastic potential.

4. Conclusion

In this research, the damage formation and dynamic impact behavior of elliptic curved specimen was considered. The results indicate that the targets' ability to absorb energy in elastic deformations determines the low-velocity impact-resistance with respect to projected delamination surface extents. The amplitude of oscillations increases with the lateral height of the target. The numerical model indicates more than one delamination propagation phase especially in case of lateral high structures which is possibly induced by normal mode deformation.

A geometric stiffening effect of curvature with respect to a point load is observed. The circumferential delamination extent is constrained by increasing curvature whereas the delamination extent in the straight cross-section of the vertex rather increases with increasing curvature. Damage localization and subsequent large deformation supports the delamination propagation along the circumference. The delamination supporting bending stresses decrease with increasing curvature. After initiation of the crack in the low-curved specimens, the crack progression takes place as larger deflection occurs and higher bending stresses prevail.

Predicted interface failure is partially smaller than in the experiment and is therefore not exactly representative for the experiment. Nevertheless, a deeper understanding of the impact behavior of curved composite structures has been achieved. Numerical calibration will improve the predictive capability whereas realistic damage initiation is crucial to predict delamination propagation and subsequently the resulting damage morphology.

To design components and structures for impact resistance, geometric effects must be fully understood. For a low velocity impact load, the size of the specimen or structure is a critical parameter for determining the dynamic response. The elastic response of the target and the amount of damage caused depends on the ability of the target to store energy elastically. The height of the specimens could be adjusted, thus the circumference between the clamping remains the same, whereby the length of the imaginary unwound bending beam remains constant despite variable curvature. This might reveal a more clear look into the geometry's influence because effects of the different natural oscillations should decrease. When using samples, the evaluation of the dynamics of complex structures should be considered.

CRediT authorship contribution statement

J. Gebhardt: Conceptualization, Methodology, Software, Formal analysis, Investigation, Data curation, Visualization, Writing – original draft, Writing – review & editing. **M. Schlamp:** Resources, Project administration, Funding acquisition, Writing – review & editing. **I. Ehrlich:** Writing – review & editing, Supervision. **S. Hiermaier:** Writing – review & editing.

Declaration of competing interest

The authors declare the following financial interests/personal relationships which may be considered as potential competing interests: Ingo Ehrlich reports financial support was provided by Federal Ministry of Economics and Energy of Germany.

Data availability

Data will be made available on request.

Acknowledgments

This research work and its results are part of the project BIRD (project number ZF4114501EB5), funded by the Federal Ministry of Economics and Energy of Germany. This research work and its results are part of the project BIRD (project number ZF4114501EB5), funded by the Federal Ministry of Economics and Energy of Germany.

Supported by Open Access funds of the OTH Regensburg.

Proof reading by Silke van Schwartzenberg.

References

[1] Davies G, Zhang X. Impact damage prediction in carbon composite structures. Int J Impact Eng 1995;16(1):149–70. http://dx.doi.org/10.1016/0734-743X(94)00039-Y.

[2] Sun XC, Hallett SR. Barely visible impact damage in scaled composite laminates: Experiments and numerical simulations. Int J Impact Eng 2017;109:178–95. http://dx.doi.org/10.1016/j.ijimpeng.2017.06.008.

[3] Olsson R. Low- and medium-velocity impact as a cause of failure in polymer matrix composites. In: Failure mechanisms in polymer matrix composites. Elsevier; 2012, p. 53–78. http://dx.doi.org/10.1533/9780857095329.1.53.

[4] Richardson M, Wisheart MJ. Review of low-velocity impact properties of composite materials. Composites A 1996;27(12):1123–31. http://dx.doi.org/10.1016/1359-835X(96)00074-7.

[5] Choi HY, Wu H-YT, Chang F-K. A new approach toward understanding damage mechanisms and mechanics of laminated composites due to low-velocity impact: Part II—Analysis: Part II - analysis. J Compos Mater 1991;25(8):1012–38. http://dx.doi.org/10.1177/002199839102500804.

[6] Ehrlich I, Dinnebier H, Jost C. Comparison of impact delaminations in CFRP using different test methods. J Achiev Mater Manuf Eng 2015;73(2):128–38, URL http://jamme.acmsse.h2.pl/vol73_2/73212.pdf.

[7] Ambur D, Starnes J. Effect of curvature on the impact damage characteristics and residual strength of composite plates. In: Ko J, Strganac TW, Kurdila AJ, editors. 39th AIAA/ASME/ASCE/AHS/ASC structures, structural dynamics, and materials conference and exhibit. Reston, Virigina: American Institute of Aeronautics and Astronautics; 1998, http://dx.doi.org/10.2514/6.1998-1881.

[8] Krishnamurthy KS, Mahajan P, Mittal RK. Impact response and damage in laminated composite cylindrical shells. Compos Struct 2003;59(1):15–36. http://dx.doi.org/10.1016/S0263-8223(02)00238-6.

[9] Kim SJ, Goo NS, Kim TW. The effect of curvature on the dynamic response and impact-induced damage in composite laminates. Compos Sci Technol 1997;57(7):763–73. http://dx.doi.org/10.1016/S0266-3538(97)80015-2.

[10] Kumar S, Nageswara Rao B, Pradhan B. Effect of impactor parameters and laminate characteristics on impact response and damage in curved composite laminates. J Reinf Plast Compos 2007;26(13):1273–90. http://dx.doi.org/10.1177/0731684407079367.

[11] Saghafi H, Minak G, Zucchelli A. Effect of preload on the impact response of curved composite panels. Composites B 2014;60:74–81. http://dx.doi.org/10.1016/j.compositesb.2013.12.026.

[12] Short G, Guild F, Pavier M. Post-impact compressive strength of curved GFRP laminates. Composites A 2002;33(11):1487–95. http://dx.doi.org/10.1016/S1359-835X(02)00175-6.

[13] Bogenfeld R, Kreikemeier J, Wille T. Review and benchmark study on the analysis of low-velocity impact on composite laminates. Eng Fail Anal 2018.

[14] Faggiani A, Falzon BG. Predicting low-velocity impact damage on a stiffened composite panel. Composites A 2010;41(6):737–49. http://dx.doi.org/10.1016/j.compositesa.2010.02.005.

[15] Ganapathy S, Rao KP. Failure analysis of laminated composite cylindrical/spherical shell panels subjected to low-velocity impact. Comput Struct 1998;68(6):627–41. http://dx.doi.org/10.1016/S0045-7949(98)00080-7.

[16] Georgiadis S, Gunnion AJ, Thomson RS, Cartwright BK. Bird-strike simulation for certification of the boeing 787 composite moveable trailing edge. Compos Struct 2008;86(1–3):258–68. http://dx.doi.org/10.1016/j.compstruct.2008.03.025.

[17] Riccio A, Cristiano R, Saputo S, Sellitto A. Numerical methodologies for simulating bird-strike on composite wings. Compos Struct 2018;202:590–602. http://dx.doi.org/10.1016/j.compstruct.2018.03.018.

[18] Schoeppner GA, Abrate S. Delamination threshold loads for low velocity impact on composite laminates. Composites A 2000;31(9):903–15. http://dx.doi.org/10.1016/S1359-835X(00)00061-0.

[19] Hashin Z, Rotem A. A fatigue failure criterion for fiber reinforced materials. J Compos Mater 1973;7(4):448–64. http://dx.doi.org/10.1177/002199837300700404.

[20] Choi HY, Chang F-K. A model for predicting damage in graphite/epoxy laminated composites resulting from low-velocity point impact. J Compos Mater 1992;26(14):2134–69. http://dx.doi.org/10.1177/002199839202601408.

[21] Choi HY, Downs RJ, Chang F-K. A new approach toward understanding damage mechanisms and mechanics of laminated composites due to low-velocity impact: Part I—Experiments: Part I - experiments. J Compos Mater 1991;25(8):992–1011. http://dx.doi.org/10.1177/002199839102500803.

[22] Chang F-K, Chang K-Y. A progressive damage model for laminated composites containing stress concentrations. J Compos Mater 1987;21(9):834–55. http://dx.doi.org/10.1177/002199838702100904.

[23] Chang F-K, Chang K-Y. Post-failure analysis of bolted composite joints in tension or shear-out mode failure. J Compos Mater 1987;21(9):809–33. http://dx.doi.org/10.1177/002199838702100903.

[24] Ehrlich I. Impactverhalten schwach gekrümmter strukturen aus faserverstärkten kunststoffen (Doctoral thesis), Neubiberg: Universität der Bundeswehr München; 2004, URL https://d-nb.info/973886102/34.

[25] EN 6038:2015: Aerospace series - fibre reinforced plastics - test method - determination of the compression strength after impact. European Comittee for Standardization; 2016.

[26] ASTM International. ASTM D7136/D7136M - 15: Test method for measuring the damage resistance of a fiber-reinforced polymer matrix composite to a drop-weight impact event. 2015, http://dx.doi.org/10.1520/D7136_D7136M-12.

[27] SGL Group. Prepregs aus carbon-, glas- und aramidfasern: Unidirektionales epoxid-glasfaser-prepreg. 2016, URL https://www.sglcarbon.com/.

[28] DIN Deutsches Institut für Normung eV. DIN EN ISO 1172:1998-12, textilglasverstärkte kunststoffe_- prepregs, formmassen und laminate_- bestimmung des textilglas- und mineralfüllstoffgehalts; kalzinierungsverfahren. 1998, http://dx.doi.org/10.31030/8003549.

[29] Belytschko T, Bindeman LP. Assumed strain stabilization of the eight node hexahedral element. Comput Methods Appl Mech Engrg 1993;105(2):225–60. http://dx.doi.org/10.1016/0045-7825(93)90124-G.

[30] LSTC. LS-DYNA theory manual: 06/08/22 (r:14765) LS-DYNA dev. 2022, URL https://ftp.lstc.com/anonymous/outgoing/jday/manuals/DRAFT_Theory.pdf.

[31] LSTC. LS-DYNA keyword user's manual: volume I: LS-DYNA R11 10/18/18 (r:10580). 2018, URL https://ftp.lstc.com/anonymous/outgoing/jday/manuals/LS-DYNA_Manual_Volume_I_R11.pdf.

[32] LSTC. LS-DYNA keyword user's manual: volume II material models: LS-DYNA R11 02/18/19 (r:10850). 2019, URL https://ftp.lstc.com/anonymous/outgoing/jday/manuals/LS-DYNA_Manual_Volume_II_R11_Ver2.pdf.

[33] Hou JP, Petrinic N, Ruiz C, Hallett SR. Prediction of impact damage in composite plates. Compos Sci Technol 2000;60(2):273–81. http://dx.doi.org/10.1016/S0266-3538(99)00126-8.

[34] Schlamp M. Der einfluss elliptischer Krümmung auf das Verformungs- und Schädigungsverhalten glasfaserverstärkter Kunststoffstrukturen (Doctoral thesis), Freiburg: Technische Fakultät; 2022, http://dx.doi.org/10.6094/UNIFR/228064.

[35] Liu D. Impact-induced delamination—A view of bending stiffness mismatching. J Compos Mater 1988;22(7):674–92. http://dx.doi.org/10.1177/002199838802200706.